MOUNT ALLISON UNIVERSITY

Improving the Contrast of Neutron Interferometry Phase Measurements Using Online Bayesian Markov Chain Monte Carlo Methods (Super Tentative Crappy Title)

by

Thomas Alexander

A thesis submitted in partial fulfillment for the
degree of Bachelor of Science with Honours

in the

Faculty of Science
Department of Physics

March 2014

Declaration of Authorship

I, Thomas Alexander, declare that this thesis titled, 'THESIS TITLE' and the work presented in it are my own. I confirm that:

- This work was done wholly or mainly while in candidature for a research degree at this University.
- Where any part of this thesis has previously been submitted for a degree or any other qualification at this University or any other institution, this has been clearly stated.
- Where I have consulted the published work of others, this is always clearly attributed.
- Where I have quoted from the work of others, the source is always given. With the exception of such quotations, this thesis is entirely my own work.
- I have acknowledged all main sources of help.
- Where the thesis is based on work done by myself jointly with others, I have made clear exactly what was done by others and what I have contributed myself.

Signed: _____

Date: _____

"Such is the vastness of his genius that he can outwit even himself."

Steven Erikson

MOUNT ALLISON UNIVERSITY

Abstract

Faculty of Science
Department of Physics

Bachelors of Science with Honours

by Thomas Alexander

The Thesis Abstract is written here (and usually kept to just this page). The page is kept centered vertically so can expand into the blank space above the title too...

Acknowledgements

The acknowledgements and the people to thank go here, don't forget to include your project advisor...

Contents

List of Figures

List of Tables

Abbreviations

t	transmitted beam amplitude coefficient
r	reflected beam amplitude coefficient

Physical Constants

$$\text{Speed of Light} \quad c \quad = \quad 2.997\ 924\ 58 \times 10^8\ \frac{m}{s}$$

Symbols

k	quantum wave number	m^{-1}
v	velocity	ms^{-1}
ω	angular frequency	rads^{-1}

For/Dedicated to/To my...

Chapter 1

Introduction

1.1 Neutron Interferometry

1.1.1 History

Interferometry has long been a powerful tool for experimental physics. Its various forms have been used in the discovery of many historically significant results such as the Michelson-Morley experiment which showed that the speed of light was independent of inertial reference frames and experimental data in support of Bell's Inequality. [1][2]

The key concept of interferometry is the superposition of waveforms upon each other in order to deduce meaningful physical properties from the resultant combination. If one considers two waves of identical frequency than the waves when superimposed will combine constructively when in phase and de-constructively when out of phase. The technique of interferometry can be applied to many different experimental systems, the requirement being that the interferometry medium be described as a wave mathematically. Such systems that have been used in the past include electromagnetic waves, water waves, electrons and neutrons. Although electrons and neutrons classically are described as point particles the development of quantum mechanics allows that all matter is actually described by a waveform and therefore interferometry techniques may be applied to the electron and neutron waveforms. This paper focuses primarily on neutron interferometry.

The first Neutron Interferometer with slow neutrons was constructed by Maier-Leibnitz and Springer in 1962 and was effectively equivalent to a double slit experiment. However, their interferometer was not effective for measuring physical properties of materials. In 1965 the perfect single-crystal interferometer was theorized by Ulrich Bonse and Michael

Hart, however it was not until 1974 that their interferometer was made functional by Helmut Raunch and his student Wolfgang Treimer. Their interferometer used a single perfect crystal in which two horizontal slices were removed from the interior to form a three-blade interferometer.[3] **INSERT FIGURE**. Using the single-crystal design researchers Colella,Overhauser and Werner to perform the famous COW experiment which measured the phase shift due to the gravitational potential difference between two neutron beams separated by a small displacement in height.[4] Further experiments made such contributions to experimental physics such as the measurement of the Aharonov-Bohm effect and the the effect of the Earth's rotation on a quantum system.[3] It was quickly realized that neutron interferometry measurements provide an incredible level of accuracy and isolation in experimental measurements. This is due to the fact that the neutron has essentially zero electric charge and therefore does not feel the Coulomb force. Therefore for the case of slow neutrons there is no need to isolate for stray electric fields.

1.1.2 Application to Quantum Information

As the neutron interferometry provides a low-noise experimental system it provides an ideal test-bench for testing certain aspects of quantum information theory. Such an example was the use of a five-blade interferometer which allowed the quantum information encoded in the neutron waveform by using additional blades to exploit the symmetry of mechanical vibrations in the interferometer and decouple these modes.[5]. This is an example of encoding the information into a decoherence-free subspace and is a technique that may be applicable in future scalable quantum computation systems. Additionally it has been shown that neutron interferometers can be used for the generation of single neutron entangled states. [6] Additionally there is interest in the quantum discord of neutron interferometry systems and there application towards non-classical discord algorithms.[7]. It is unlikely that a scalable quantum computer will be realizable with neutrons due to their low interaction with other quantum systems.

1.1.3 Application to Quantum Fundamentals

Neutron interferometry has played a large role in experimentally gathering information on the fundamental behaviour of quantum systems. Such as the Aharonov-Bohm effect, the effect of gravity,quantum discord and verifying Bell's Inequality. [3][4][7][2]. More recently researchers at the Institute for Quantum Computing are designing an experimental neutron interferometer that is equivalent to a triple-slit experiment in the search

for third order interference effects that are theoretically non-existent but if found may be evidence of new quantum theories.[8]

1.1.4 National Institute of Standards and Technology

The majority of the work presented in this thesis applies directly to the neutron interferometry setup at the National Institute of Standards and Technology in Gaithersburg, MD. The neutrons are produced at the NIST Research Reactor and extracted via a dual-crystal parallel-tracking monochromator with energy of $4 - 20meV$. They are fed along wave-guides to the isolated interferometry setup. NIST has three,four and five blade perfect single-crystal interferometry assemblies although we focus on solely the three blade assembly. Neutron detection is provided by ^3He detectors or by high resolution position-sensitive detectors.[9][10] **INSERT FIGURES**.

1.2 Bayesian Markov Chain Monte Carlo Methods

Chapter 2

Theory

2.1 Neutrons

2.1.1 Particle Description of Neutrons

The neutron is a subatomic hadron particle that is present in the nucleus of every atom except ^1H. The neutron is composed of two down quarks and a single up quarks. This composition gives a neutral electric charge for the neutron making it an ideal candidate for sensitive experiments, however the downside is that neutrons are much more difficult to manipulate. The neutron is also therefore a fermion and by the Pauli exclusion principle only a single neutron is allowed in each quantum state. The free neutron is unstable and undergoes beta decay with a lifetime of just $881.5 \pm 1.5s$. The neutron has a rest mass of approximately $939.56Mev$. Free neutrons are produced using either neutral fission or fusion although in practical experiments fission is almost always used. At the NIST Research Reactor free neutrons are produced from the fission of ^{235}U.

2.1.2 Thermal Neutrons

Neutron interferometry utilizes thermal neutrons which are free neutrons that follow a Boltzmann distribution. The neutrons at NIST are found in the kinetic energy range of 4-20meV around room temperature of $T = 293.15K$. This gives gives neutron velocities of $875 - 1956\frac{m}{s}$ which gives $v << c$ and therefore relativistic affects do not play a role. Therefore thermal neutrons are in near thermal equilibrium with their surroundings. Neutrons are decelerated to a thermal state in the reactor by collisions with neutron moderators in the reactor. From de Broglie relations the wavelength of thermal neutrons is approximately $\lambda = \frac{h}{p} =$ 2.0-4.5$\mathring{A}$. After being emitted form the NIST reactor the

neutrons follow a wave-guide and using a wave splitter are sent into individual labs. As the strongest known phase space density of a neutron source is around $10^{-}14$ it can be safely assumed that the probability of two neutrons interacting inside the wave-guide or interferometer is sufficiently low that it can be disregarded and therefore detected neutrons have no correlation between each-other.

2.2 Neutron Interferometry

The Neutron interferometer is similar to other forms of interferometry in which an incoming wave is split and than allowed to interfere at a later point which allows the two wave paths to be compared. The modern day neutron interferometer is functionally equivalent to an optical Mach-Zender (MZ) interferometer.

2.2.1 Mach-Zehnder Interferometer

The MZ utilizes a half-mirror to split the incoming electromagnetic wave and the resultant two beam paths are refocused on a second beam-splitter. The two interfered waveforms exit the second beam-splitter and are incident on two detectors that can be visualized as Detector 1 & 2 in fig(2.1),

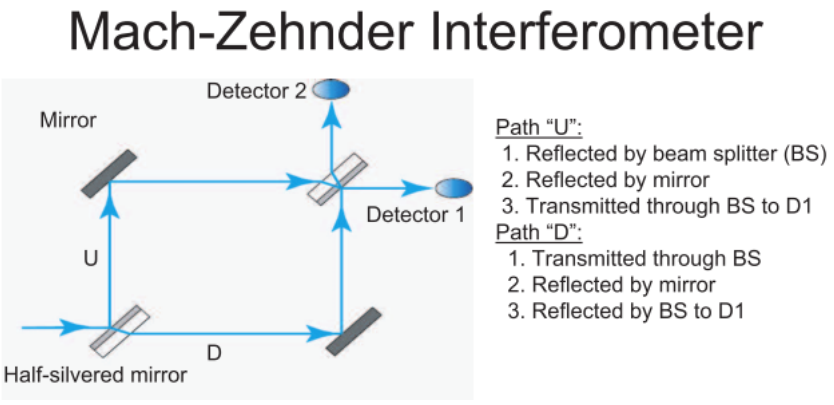

FIGURE 2.1: The Mach-Zehnder interferometer

As reflection results in a phase shift of π and assuming transmission through the half-mirrors results in a phase shift of δ we easily calculate the phase differences of the two paths at the two detectors. At detector 1 and path U there is a total of two reflections and a single transmission which results in a phase shift of $2\pi + \delta$. Similarly for path D the phase shift is also $2\pi + \delta$. therefore at detector 1 there is constructive interference. At detector 2 path U has a phase of $2\pi + 2\delta$ and path D has a phase of $\pi + 2\delta$. Therefore at detector 2 there is destructive interference.[11]

2.2.2 Bragg Scattering

In neutron interferometry the crystal planes of the interferometer blades act as diffraction gratings. Incident waves that satisfy the Bragg condition 2.1 are coherently scattered.

$$n\lambda = 2dsin(\theta_b) \tag{2.1}$$

Where n is a positive integer, d is the distance between the atomic planes of the crystal lattice and θ_b is the angle between the incident beam and the atomic plane of the crystal. The amplitudes of the transmitted and the reflected beams are given by the coefficients t (transmitted) and r reflected.[11]

2.2.3 Quantum Scattering Theory

Starting with the assumption the Hamiltonian has the form of

$$\mathcal{H} = \mathcal{H}_0 + \mathcal{V} \quad \mathcal{H}_0 = \frac{\mathbf{p}^2}{2m} \tag{2.2}$$

The presence of the potential $\mathcal{V}$ causes the solution to be different than the free particle state

$$\mathcal{H}_0 \left|\Phi\right\rangle = E \left|Phi\right\rangle$$

Therefore we are looking for solutions to the Schrdinger equation of the form

$$\mathcal{H}_0 + \mathcal{V} \left|\Psi\right\rangle = E \left|\Psi\right\rangle \tag{2.3}$$

A valid solution should have that $\left|\Psi\right\rangle \to \left|\Phi\right\rangle$ as $\mathcal{V} \to 0$. A solution that satisfies these requirements is known as the Lippmann-Schwinger equation.

$$\left|\Psi^{\pm}\right\rangle = \left|\Phi\right\rangle + \frac{1}{E - \mathcal{H}_0 \pm i\epsilon}\mathcal{V}\left|\Psi^{\pm}\right\rangle \tag{2.4}$$

Here the energy E was made slightly complex with the addition of $\pm\epsilon$ to deal with the singular nature of the operator $1/(E - \mathcal{H}_0)$. It can easily be seen that the application of the operator $E - \mathcal{H}_0$ reduces (2.4) to the desired solution (2.3) when neglecting the imaginary component. By taking the Lipmann-Schwinger equation to the position basis explicitly it can be represented as

$$\left\langle \boldsymbol{x} \,\middle|\, \Psi^{\pm} \right\rangle = \left\langle \boldsymbol{x} \,\middle|\, \Phi \right\rangle - \frac{2m}{\hbar^2} \int d^3x' \frac{e^{\pm ik\left|\boldsymbol{x} - \boldsymbol{x}'\right|}}{4\pi\left|\boldsymbol{x} - \boldsymbol{x}'\right|} \left\langle \boldsymbol{x}' \,\middle|\, \mathcal{V} \,\middle|\, \Psi^{\pm} \right\rangle \tag{2.5}$$

As our scattering potentials are a function of position only the assumption can be made that the potential is *local* such that it is diagonal in the position representation. Specifically the potential satisfies the requirement that

$$\langle \boldsymbol{x}^{'} | \mathcal{V} | \boldsymbol{x}^{''} \rangle = \mathcal{V}(\boldsymbol{x}^{'}) \delta^{(3)}(\boldsymbol{x}^{'} - \boldsymbol{x}^{''}) \tag{2.6}$$

Utilizing this potential we obtain

$$\left\langle \boldsymbol{x} \,\middle|\, \mathcal{V} \,\middle|\, \Psi^{\pm} \right\rangle = \int d^3x^{''} \, \langle \boldsymbol{x}^{'} | \mathcal{V} | \boldsymbol{x}^{''} \rangle \, \langle \boldsymbol{x}^{''} | \Psi^{\pm} \rangle = \mathcal{V}(\boldsymbol{x}^{'}) \, \langle \boldsymbol{x}^{'} | \Psi^{\pm} \rangle \tag{2.7}$$

With this result the Lippmann-Schwinger equation can be reduced to

$$\left\langle \boldsymbol{x} \,\middle|\, \Psi^{\pm} \right\rangle = \langle \boldsymbol{x} \,|\, \Phi \rangle - \frac{2m}{\hbar^2} \int d^3x^{'} \frac{e^{\pm ik \left| \boldsymbol{x} - \boldsymbol{x}^{'} \right|}}{4\pi \left| \boldsymbol{x} - \boldsymbol{x}^{'} \right|} \mathcal{V}(\boldsymbol{x'}) \left\langle \boldsymbol{x}^{'} \,\middle|\, \Psi^{\pm} \right\rangle \tag{2.8}$$

Given that we are concerned with studying finite range scatters and that any observations that will be made will be made outside the range of the potential due to the macroscopic nature of neutron detectors the assumption can be made that $|\boldsymbol{x}| >> \left| \boldsymbol{x}^{'} \right|$.

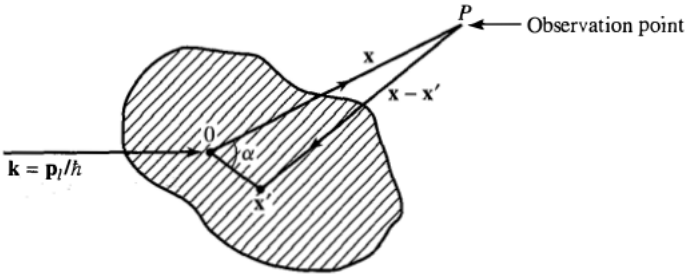

FIGURE 2.2: The finite range scattering potential. Any observations via detectors will be outside the range of the potential and therefore approximations can be made when evaluating (2.8).

Keeping in mind this result we can define

$$r = |\boldsymbol{x}|$$

$$r^{'} = \left| \boldsymbol{x}^{'} \right|$$

$$\alpha = \angle(\boldsymbol{x}, \boldsymbol{x}^{'})$$

$$\hat{\boldsymbol{r}} \equiv \frac{\boldsymbol{x}}{|\boldsymbol{x}|}$$

$$\left|\boldsymbol{x}-\boldsymbol{x}^{'}\right| \approx r-\hat{\boldsymbol{r}}\cdot\boldsymbol{x}^{'} \tag{2.9}$$

$$\boldsymbol{k}^{'} \equiv k\hat{\boldsymbol{r}} \tag{2.10}$$

Utilizing equations (2.9,2.10)

$$e^{\pm ik\left|\boldsymbol{x}-\boldsymbol{x}^{'}\right|} \approx e^{\pm ikr}e^{\mp i\boldsymbol{k}^{'}\cdot\boldsymbol{x}^{'}} \tag{2.11}$$

For the distant r at the observation point it is a useful approximation to say that

$$\frac{1}{\left|\boldsymbol{x}-\boldsymbol{x}^{'}\right|} \approx \frac{1}{r} \tag{2.12}$$

Now replacing our incident generic wave with an incident plane wave $|\Phi\rangle \rightarrow |\boldsymbol{p}\rangle$ and using $\boldsymbol{k} \equiv \boldsymbol{p_i}/\hbar$ To remove the $\hbar$'s from the expression. We obtain for the first term in (2.8)

$$\langle \boldsymbol{x} \,|\, \boldsymbol{k}\rangle = \int d^3k^{'} \left\langle \boldsymbol{x} \,\middle|\, \boldsymbol{k}^{'}\right\rangle \left\langle \boldsymbol{k}^{'} \,\middle|\, \boldsymbol{k}\right\rangle = \int d^3k^{'} \left\langle \boldsymbol{x} \,\middle|\, \boldsymbol{k}^{'}\right\rangle \delta^{(3)}(\boldsymbol{k}^{'}-\boldsymbol{k}) = \frac{e^{i\boldsymbol{k}\cdot\boldsymbol{x}}}{(2\pi)^{\frac{3}{2}}} \tag{2.13}$$

Using this result in (2.8) gives an expression for the scattered wave function at a relatively distant observation point for the positive Lippmann-Schwinger wavefunction.

$$\left\langle \boldsymbol{x} \,\middle|\, \Psi^{+}\right\rangle = \frac{1}{(2\pi)^{\frac{3}{2}}}\left(e^{i\boldsymbol{k}\cdot\boldsymbol{x}} + \frac{e^{ikr}}{r}f(\boldsymbol{k}^{'},\boldsymbol{k})\right) \tag{2.14}$$

$$f(\boldsymbol{k}^{'},\boldsymbol{k}) = -m\left(\frac{2\pi}{h}\right)^2 \left\langle \boldsymbol{k}^{'} \,\middle|\, \mathcal{V} \,\middle|\, \Psi^{+}\right\rangle \tag{2.15}$$

It is very easy to see that the result wavefunction is a combination of the original incident plane-wave and an outgoing spherical wave with an amplitude described by (2.15). An obvious issue is that here scattering has only been treated for an incident plane-wave which is not a normalizable wavefunction. In reality to describe discrete particles such as neutrons wave packet solutions are used to describe the incident particles. However, provided the size of the wave packet is much larger than the range of the finite potential $\mathcal{V}$ it is sufficient to treat an incident packet as a plane-wave.

2.2.4 Differential Cross-Section

The scattering cross section is an important parameter for experimental scattering physics. It relates the number of particles scattering into the solid angle $d\Omega$ per unit time to the number of incident particles into an infinitesimal element $d\sigma$ of area per unit

time. We search for a relation between $d\Omega$ and $d\sigma$ which we term the differential cross section given by $d\sigma/d\Omega$. Evidently the probability of an incident particle being within

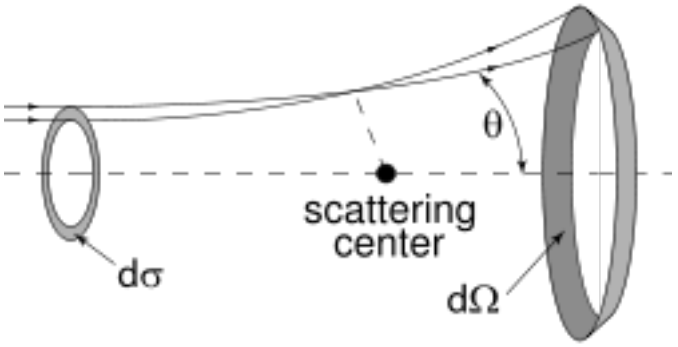

FIGURE 2.3: The differential cross section is the relationship between incident particles travelling through area $d\sigma$ to scattered particles crossing through the solid angle $d\Omega$

an area $d\sigma$ in time dt while travelling with velocity v is just

$$dP = |\Psi_i|^2 \, dV = \frac{1}{2\pi}^3 (vdt)d\sigma \tag{2.16}$$

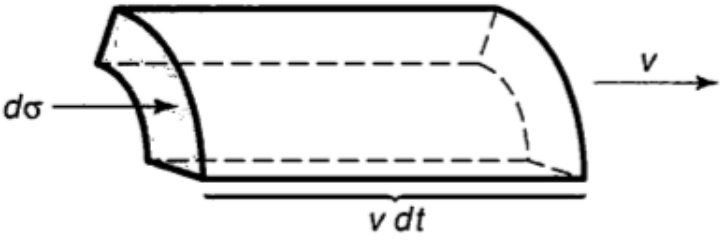

FIGURE 2.4: The volume element dV that a beam occupies passing through an area $d\sigma$ in time dt

Relating this probability to the probability of a particle being scattered into solid angle $d\Omega$ with equal velocity v per unit time dt.

$$dP = |\Psi_s|^2 \, dV = \frac{1}{2\pi}^3 \frac{\left|f(\boldsymbol{k'}, \boldsymbol{k})\right|^2}{r^2} (vdt) r^2 d\Omega \tag{2.17}$$

Equations (2.16) and (2.17) can be solved for the differential cross section

$$\frac{d\sigma}{d\Omega} = \left|f(\boldsymbol{k'}, \boldsymbol{k})\right|^2 \tag{2.18}$$

2.2.5 Scattering Amplitude

While equation (2.15) defines the magnitude of the outgoing spherical wave, it is defined implicitly in terms of the unknown ket $|\Psi^+\rangle$. The solution to this problem in the case

of sufficiently weak scatterers is to use the first Born approximation

$$\left\langle \boldsymbol{x}^{'} \middle| \Psi^{+} \right\rangle \rightarrow \left\langle \boldsymbol{x}^{'} \middle| \Phi \right\rangle = \frac{e^{i\boldsymbol{x}^{'}}}{(2\pi)^{3/2}} \tag{2.19}$$

Combining (2.19) and (2.15) results in the first-order Born amplitude

$$f^{(1)}(\boldsymbol{k}^{'}, \boldsymbol{k}) = -\frac{m}{2\pi\hbar^2} \int d^3x^{'} e^{i(\boldsymbol{k}-\boldsymbol{k}^{'})\cdot\boldsymbol{x}^{'}} \mathcal{V}(\boldsymbol{x}^{'}) \tag{2.20}$$

As the potentials that will be dealt with are spherically symmetrical, further approximations can be made utilizing $\boldsymbol{q} \equiv \boldsymbol{k} - \boldsymbol{k}^{'}$ and

$$\left|\boldsymbol{k} - \boldsymbol{k}^{'}\right| \equiv q = 2ksin\left(\frac{\theta}{2}\right)$$

as seen in fig(2.5) The spherical symmetry can be used to integrate explicitly the angular component of the scattering magnitude.

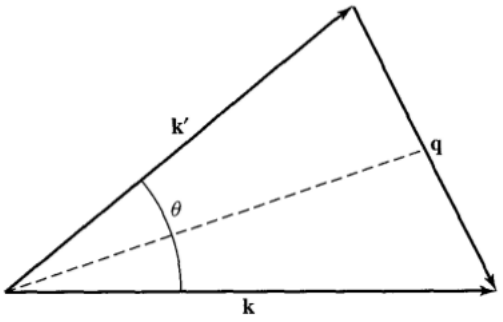

FIGURE 2.5: Scattering amplitude as a function of θ where $\boldsymbol{q} = \boldsymbol{k} - \boldsymbol{k}^{'}$

$$f^{(1)}(\theta) = -\frac{m}{2\pi\hbar^2} \int_{r=0}^{\infty} \int_{\phi=0}^{2\pi} \int_{\theta'=0}^{\pi} e^{i|q||r|cos(\theta^{'})} sin(\theta^{'}) r^2 \mathcal{V}(r) d\theta^{'} d\phi dr$$

$$= -\frac{1}{2i}\frac{2m}{\hbar^2 q} \int_0^{\infty} r\mathcal{V}(r)(e^{iqr} - e^{-iqr})dr = -\frac{2m}{\hbar^2}\frac{1}{q} \int_0^{\infty} r\mathcal{V}(r)sin(qr)dr \tag{2.21}$$

Given a potential that has spherical symmetry it is now much more simple to calculate the scattering amplitude using (2.21).

2.2.6 Neutron-nucleus Scattering

Generally there are two interactions that an incident neutron on a material will experience. The interaction with the nucleus of the material atoms and which is referred to as nuclear scattering and the scattering due to interaction with unpaired electrons

and their magnetic moments which is known as magnetic scattering. In practice nuclear scattering is more common as it allows the structure of solids to probed.

Given the assumptions that an incoming neutron beam will be elastically scattered and that the nucleus is fixed, the scattering will depend on the potential $V(\boldsymbol{r})$ between the nucleus and neutron. As this is interaction is due to the strong-force it is naturally occurring over a very short range, and is approximately zero at a distance of the order $\boldsymbol{r} = 10^{-15}m$. As this is much shorter than the wavelength of thermal and cold neutrons which are used in almost all scattering experiments, the nucleus acts as a point scatterer. A neutron beam can be represented as a plane wave a wave function described by (2.13) and the scattered wavefunction will take the form of (2.14,2.15).

Due to the magnitude of the difference between the wavelength of the incident neutrons and the effective acting distance of the strong-force neutron-nucleus interaction and its approximate spherical symmetry it is an acceptable approximation to use the Fermi pseudo-potential

$$\mathcal{V}(\boldsymbol{x}') = \frac{2\pi\hbar^2}{m} b\delta(\boldsymbol{x}') \tag{2.22}$$

as a scattering potential. Where b is known as the neutron scattering length and his units of meters. For the case of multiple nuclei the potential takes the form

$$\mathcal{V}(\boldsymbol{x}') = \frac{2\pi\hbar^2}{m} \sum_j b_j \delta(\boldsymbol{x}' - \boldsymbol{x_j}) \tag{2.23}$$

Using the spherical approximate Born solution for the amplitude (2.20) and the Fermi pseudo-potential the scattering amplitude can be found to be

$$f^{(1)}(\theta) = -\int d^3x' e^{i(\boldsymbol{k} - \boldsymbol{k}')\cdot\boldsymbol{x}'} \sum_j b_j \delta(\boldsymbol{x}' - \boldsymbol{x_j}) = -\sum_j b_j e^{i(\boldsymbol{q} \cdot \boldsymbol{x_j}} \tag{2.24}$$

And in the case of a single scatterer at the origin reducing to

$$f^{(1)}(\theta) = -b \tag{2.25}$$

Therefore it can be seen that the completed neutron scattered wave form is

$$\langle \boldsymbol{x} \mid \Psi^+ \rangle = \frac{1}{(2\pi)^{\frac{3}{2}}} \left(e^{i\boldsymbol{k} \cdot \boldsymbol{x}} - \sum_j b_j e^{i(\boldsymbol{q} \cdot \boldsymbol{x_j}} \frac{e^{ikr}}{r} \right) \tag{2.26}$$

From this approximate solution it is evident that the only difference between individual scatterers is their neutron scattering length b. The value b varies greatly among even neighbouring elements in the periodic table. Unfortunately the outlined theory is not

strong enough to predict the scattering length and the parameters must be determined experimentally.

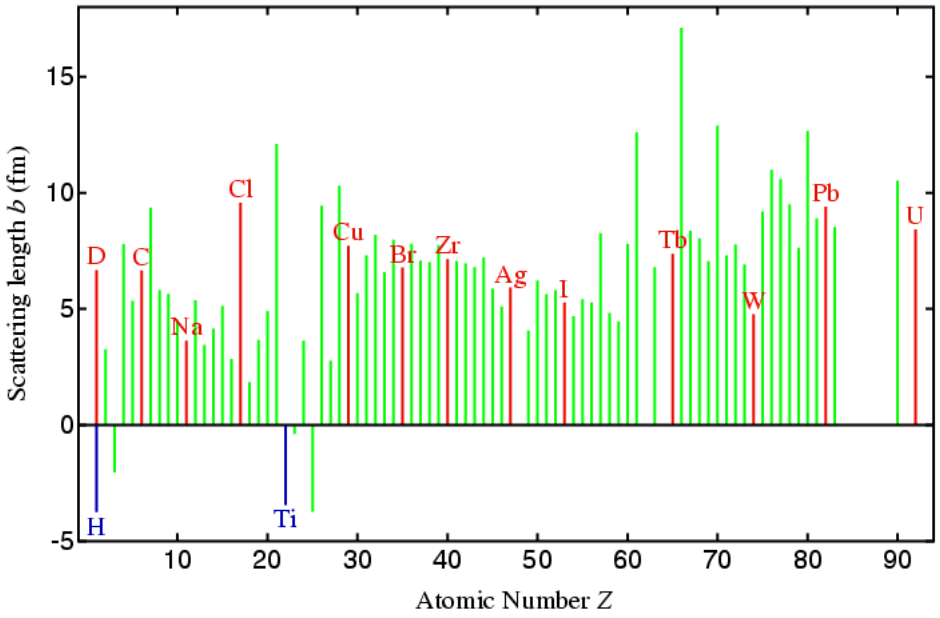

FIGURE 2.6: Neutron scattering lengths b for the elements of the periodic table

Inside a sufficiently large homogeneous material the Fermi pseudo-potential can be approximated to be

$$\mathcal{V}(\boldsymbol{x}') = \frac{2\pi\hbar^2}{m}\sum_j b_j\delta(\boldsymbol{x}' - \boldsymbol{x_j}) \approx \frac{2\pi\hbar^2}{m}bN \tag{2.27}$$

Where N is the atom number density.

2.2.7 Neutron Optics

As the neutron beam is a wavefunction many analogies from classical optics hold. The index of refraction is defined as the ratio of the speed of neutrons experiencing no potential to the speed of neutrons affected by a potential. Compared to light the form is familiar

$$\frac{c}{n} = \frac{K}{k}$$

Where from Schrdinger's equation

$$\Delta^2\Psi(\boldsymbol{x}) + \frac{2m}{\hbar^2}(E - \mathcal{V}(\boldsymbol{x})\Psi(r) = 0$$

$$K^2 = \frac{2m}{\hbar^2}(E - \mathcal{V}(\boldsymbol{x})) \tag{2.28}$$

$$n(\boldsymbol{x}) = \frac{K}{k} = \sqrt{\frac{E - \mathcal{V}(\boldsymbol{x})}{E}} = \sqrt{1 - \frac{\mathcal{V}(\boldsymbol{x})}{E}} \tag{2.29}$$

Given that the neutron scattering potentials are described by (2.27) the index of refraction can be approximated to

$$V(\boldsymbol{x}) = \sqrt{1 - \frac{\frac{2\pi\hbar^2}{m} bN}{E}} \tag{2.30}$$

In the case of magnetic materials the magnetic potential

$$\mathcal{V}_{mag}(\boldsymbol{x}) = -\boldsymbol{u} \cdot \boldsymbol{B_{eff}}$$

must be accounted for. This results in an index of refraction for magnetic materials such as Fe,Ni and Co of

$$n_{\pm}(\boldsymbol{x}) = \sqrt{1 - \frac{\frac{2\pi\hbar^2}{m} bN \mp \boldsymbol{u} \cdot \boldsymbol{B_{eff}}}{E}} \tag{2.31}$$

2.2.8 Neutron Wave Guides

Chapter 3

Experimental Setup

3.1 The Neutron Interferometer

The neutron interferometer that this thesis refers to is located at the Neutron Interferometry and Optics facility (NIOF) at the National Institute of Standards and Technology (NIST) in Gaithersburg, MD.

3.1.1 NIST

3.1.2 Reactor

NIST operates a 20MW split-core research reactor. Neutrons of approximate energy $1MeV$ are emitted during ^{235}U fission and then thermalized using heavy water (D_2O) as a moderator. This brings the neutrons to room temperature as discussed in (2.1.2). At the reactor core the peak thermal neutron flux is $4 \times 10^{14} neutrons/cm^2$. The reactor is operated on a seven week cycle during which it is operated at full power for 38 days and then followed by 11 days of refuelling and maintenance operations.

As the longer wavelength of cold neutrons ($\lambda > 1.8\mathring{A}$ and $E < 25meV$) is often desired for condensed matter study there is a cold moderator installed next to the core. The thermal neutrons scatter with liquid hydrogen at $20K$ and exit with a Maxwellian distribution of characteristic temperature of $34K$.

There are eight thermal neutron ports available for lab use. The neutrons are transported to the instruments in the NCNR hall using neutron guides. The neutron interferometer facility is located on the NG7 guide shown in figure (**??**). The guides are of a rectangular cross-section and are produced by gluing together meter long sections of $100nm$ thick

^{58}Ni optically-flat borated glass plates. ^{58}Ni is used due to its large neutron reflective potential.

$$V = \frac{2\pi * \hbar^2}{m}\rho = \frac{2\pi\hbar^2}{m}\frac{1}{V}\sum_i b = 335neV$$

3.1.3 Motors and Actuators

The neutron interferometry lab uses a variety of motors and actuators that allow experimental parameters to be controlled over the wire. Depending on the device communication is achieved via analog or digital protocols.

3.1.3.1 Newport 301

The Newport ESP301 is a three axis motion controller and driver.[12] It can drive both DC servo motors and 2-phase stepper motors at up to 3 amps. It has a 1000x microstep resolution per axis which allows very fine grained control of movements which is necessary for precision measurements. The Newport ESP 301 is primarily used to drive servo motors that orient the phase flag in the neutron interferometer. Precise angular control is a must as this is one of the primary experimental parameter. The device can also be used to control the interferometry stage to orient it.

The Newport device utilizes encoder feedback built into servos to obtain precise positional feedback. While most Newport brand motors will automatically supply their configuration information, the equipment at NIST is not necessarily compatible in such a way. Therefore advanced configuration must be supplied by the device programmer.

The ESP301 is controllable via a fairly extensive language of approximately 100 commands, a large portion of which are necessary for the device to be controlled successfully. Valid configuration information must be supplied. Commands are transmitted via ASCII characters according to the selected protocol. Supported protocols are serial RS232C, USB and IEEE488 with delays of $7 - 30ms$,$3.5ms$ and $1ms$ respectively.

3.1.3.2 Kepco

Kepco series ATE power supplies are used to control a variety of devices in the interferometry lab. Specifically the 15-6M and 36-15M models are used and are rack mounted. The models are rated at (0-$15V$,0-$6A$,$50W$) and (0-$36V$,0-$15A$,$500W$) respectively.[13] The models are controllable via an analog input line that sets the supply output as a linear function of the input from 0-$10V$. Additionally there is a crowbar voltage controller

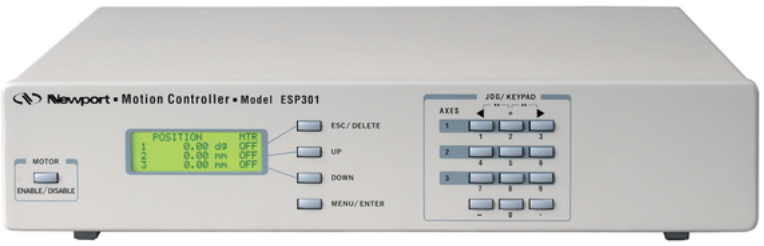

FIGURE 3.1: Newport ESP301 three axis motion controller

which allows a maximum voltage to be set in a similar manner. The Kepco supplies are controllable via DACs which are managed via a LabJack.

3.1.3.3 LabJack

The LabJack is a low cost measurement and automation platform. Specifically NIST will use the U3-LV variant. The U3-LV provides up to 16 analog inputs, 2 analog outputs and up to 20 digital I/O pins. The analog inputs accept voltages from 0-3.6V and the onboard DACs outputs from 0-5V. The LabJack devices are easily controlled via a Python API.

In Addition to the LabJack the LJTick-DACs, a DAC made to be digitally controlled by LabJack devices are used to provide control inputs to devices such as the Kepco power supplies. The LJTick-DAC outputs $\pm 10V$ controllable by the LabJack pins in which it is inserted too. Each LJTick-DAC provides two DACs.

3.1.4 Sensors

As the likelihood method for the contrast measurement is a function of the temperature and humidity of the interferometer chamber, a variety of measurements must be taken using many different sensors.

FIGURE 3.2: Labjack U3 with LJTick-DAC

3.1.4.1 EI1050 Temperature and Humidity Probe

The EI1050 is a digital temperature and humidity probe produced by LabJack. While its protocol is open source, it has been designed to be used with a LabJack device and sample code has been provided. The device is not especially accurate as it is rated at $\pm 0.5^{\circ}$ and $\pm 3.5\%$ humidity at ranges from -40-$120C$ and 0-100% humidity. It is still useful to provide a quick and easy measurement.

3.1.4.2 Stanford Research Systems CTC100 Temperature Controller

The SRS CTC100 is a cryogenic temperature controller. It provides four sensor inputs, four analog outputs and six feedback control loops. Temperature readings are made by thermistor sensors and heating is provided by resistive heaters. The device is programmable using USB, Ethernet and either GPIB or RS-232 inputs. Commands are provided via ASCII commands. The thermistor temperature readings are very accurate with an accuracy of $\pm 0.25\Omega$ for a 300Ω thermistor. The CTC100 automatically supplies the mean and standard deviation of sampled temperatures.

FIGURE 3.3: Stanford Research Systems CTC100: Cryogenic Temperature Controller

3.2 NI-Engine

3.2.1 Design Requirements

3.2.2 Language and Library Choices

3.2.3 System Architecture

3.2.4 Documentation

3.3 Q-Infer

3.3.1 Interaction with NI-Engine

3.3.2 GPU Implementations of Likelihood functions

Chapter 4

Discussion

4.1 Application to Quantum Information

4.2 Application to Quantum Fundamentals

4.3 Application to Materials Science

4.4 Outside of Neutron Interferometry

Chapter 5

Conclusion

5.1 Contrast Improvement with MCMC Methods

5.2 The Experimental Setup

5.3 Application of Findings

Bibliography

[1] A. A. Michelson and E. W. Morley. On the relative motion of the earth and the luminiferous ether. *American Journal of Science*, 34:333–345, 1887. doi: doi:10.2475/ajs.s3-34.203.333. URL http://dx.doi.org/10.1007/s10701-010-9529-9.

[2] Yuji Hasegawa, Rudolf Loidl, Gerald Badurek, Matthias Baron, and Helmut Rauch. Violation of a bell-like inequality in single-neutron interferometry. *Nature*, 425, 2003. ISSN 6953. URL http://dx.doi.org/10.1038/nature01881.

[3] A.G. Klein. Adventures in neutron interferometry. *Foundations of Physics*, 42 (1):147–152, 2012. ISSN 0015-9018. doi: 10.1007/s10701-010-9529-9. URL http://dx.doi.org/10.1007/s10701-010-9529-9.

[4] R. Colella, A. W. Overhauser, and S. A. Werner. Observation of gravitationally induced quantum interference. *Phys. Rev. Lett.*, 34:1472–1474, Jun 1975. doi: 10.1103/PhysRevLett.34.1472. URL http://link.aps.org/doi/10.1103/PhysRevLett.34.1472.

[5] D. A. Pushin, M. G. Huber, M. Arif, and D. G. Cory. Experimental realization of decoherence-free subspace in neutron interferometry. *Phys. Rev. Lett.*, 107:150401, Oct 2011. doi: 10.1103/PhysRevLett.107.150401. URL http://link.aps.org/doi/10.1103/PhysRevLett.107.150401.

[6] Yuji Hasegawa, Rudolf Loidl, Gerald Badurek, Stefan Filipp, Jürgen Klepp, and Helmut Rauch. Evidence for entanglement and full tomographic analysis of bell states in a single-neutron system. *Phys. Rev. A*, 76:052108, Nov 2007. doi: 10.1103/PhysRevA.76.052108. URL http://link.aps.org/doi/10.1103/PhysRevA.76.052108.

[7] Christopher J. Wood, David G. Cory, Mohamed O. Abutaleb, Michael G. Huber, Muhammad Arif, and Dmitry A. Pushin. Quantum correlations in a noisy neutron interferometer. Jun 2013. URL http://arxiv.org/abs/1304.6935.

[8] Cozmin Ududec, Howard Barnum, and Joseph Emerson. Three slit experiments and the structure of quantum theory. *Foundations of Physics*, 41(3):396–405, 2011.

ISSN 0015-9018. doi: 10.1007/s10701-010-9429-z. URL http://dx.doi.org/10.1007/s10701-010-9429-z.

[9] Neutron interferometry and optics facility. http://physics.nist.gov/MajResFac/InterFer/text.html. Accessed: 2014-01-27.

[10] Sam Werner. Neutron interferometry: From missouri to nist. http://webster.ncnr.nist.gov/nran/talks/Werner.pdf. Accessed: 2014-01-27.

[11] Dmitry A Pushin. *Coherent control of neutron interferometry*. PhD thesis, 2007. URL http://hdl.handle.net/1721.1/39292.

[12] Esp301 integrated 3-axis motion controller/driver, 2013. URL http://assets.newport.com/webDocuments-EN/images/14294.pdf.

[13] INC. Kepco. Series ate. URL http://www.kepcopower.com/specs/atespecs.pdf.